nature physics

LETTERS

https://doi.org/10.1038/s41567-020-0974-x

Check for updates

Visualization of the flat electronic band in twisted bilayer graphene near the magic angle twist

M. Iqbal Bakti Utama[1,2,3,10], Roland J. Koch[4,10], Kyunghoon Lee[1,3,10], Nicolas Leconte[5], Hongyuan Li[1,6], Sihan Zhao[1], Lili Jiang[1], Jiayi Zhu[1], Kenji Watanabe[7], Takashi Taniguchi[7], Paul D. Ashby[8], Alexander Weber-Bargioni[8], Alex Zettl[1,3,9], Chris Jozwiak[4], Jeil Jung[5]✉, Eli Rotenberg[4], Aaron Bostwick[4]✉ and Feng Wang[1,3,9]✉

Bilayer graphene has been predicted to host a moiré miniband with flat dispersion if the layers are stacked at specific twist angles known as the 'magic angles'[1,2]. Recently, twisted bilayer graphene (tBLG) with a magic angle twist was reported to exhibit a correlated insulating state and superconductivity[3,4], where the presence of the flat miniband in the system is thought to be essential for the emergence of these ordered phases in the transport measurements. Although tunnelling spectroscopy[5–9] and electronic compressibility measurements[10] in tBLG have found a van Hove singularity that is consistent with the presence of the flat miniband, a direct observation of the flat dispersion in the momentum space of such a moiré miniband in tBLG is still lacking. Here, we report the visualization of this flat moiré miniband by using angle-resolved photoemission spectroscopy with nanoscale resolution. The high spatial resolution of this technique enabled the measurement of the local electronic structure of the tBLG. The measurements demonstrate the existence of the flat moiré band near the charge neutrality for tBLG close to the magic angle at room temperature.

An implication of an electronic band with flat momentum-space dispersion is the singularity in the density of states, leading to atomic-like discretization of the energy levels reminiscent of the Landau levels in the quantum Hall regime. If the Fermi level (E_F) of the material is tuned to lie at these singularities, the system can prefer to reduce the total electronic ground state energy via an energy gap opening that triggers the emergence of exotic quantum phase transitions. Thus, efforts to engineer flat bands around E_F are an active research focus where major advances are being made in various lattice systems, including in the moiré superlattices with gapless and gapped Dirac Hamiltonians.

Graphitic systems are among the families of materials that can host flat electronic bands[11–17], with reports of high densities of states near van Hove singularities at high binding energies and reduction of band dispersion in rhombohedral multilayers near charge neutrality. More recently, tBLG has emerged as a promising system due to its excellent tunability: in the degree of interlayer hybridization with twist angle[18–20] and in the possibility of using in situ electrostatic gating for adjusting E_F to occupy the flat moiré minibands or to achieve commensurate filling. The quenching of quasiparticle kinetic energy following the reduced miniband bandwidth at the magic angle is conducive to the emergence of interaction-driven phase transitions. Partial filling of the flat miniband in tBLG has resulted in the observation of correlated insulator[3], superconductivity[4,21,22] and orbital magnetism[22]. Richer physics may also arise by accounting for the sample environment, such as the ferromagnetism in magic angle tBLG with alignment to the hexagonal boron nitride (hBN) substrate[23,24].

Here, we visualize the weak dispersion of the flat moiré miniband in tBLG near the magic angle twist with angle-resolved photoemission spectroscopy with nanoscale resolution (nanoARPES). ARPES provides a unique capability to resolve the k-space dispersion of the flat band. The high spatial resolution of nanoARPES enabled by the capillary focusing (~1 μm beam spot size, see Methods) is beneficial to counteract local structural inhomogeneity within the sample. The flat band is present even at room temperature near E_F around the original $\bar{K}$ points of the constituent graphene monolayers.

Figure 1a shows the configuration of the sample. The sample was fabricated via a tear-and-stack method for controlled twist angle combined with stack inversion (see Methods). This method allows production of uncapped tBLG on a flat hBN flake to minimize surface roughness (also see Supplementary Fig. 3b) and thus achieve improved momentum resolution during the photoemission spectroscopy. Figure 1b is an optical image of such a graphene sample on hBN, where the borders of the isolated monolayers and the tBLG region are indicated as determined from atomic force microscopy (AFM) in Fig. 1c. Scanning photoemission microscopy (SPEM; Fig. 1d,e) that maps the real space distribution of generated photoelectrons from the valence band of graphene and hBN confirms the sample configuration. The intensity of the signal arising from graphene correlates with the layer number: the middle region has a stronger signal than the two sandwiching regions, matching the expected location of the monolayer and tBLG segments as demarcated in Fig. 1b. Similarly, the reduction of the hBN signal also correlates qualitatively with the attenuation from the different graphene thickness at each segment.

[1]Department of Physics, University of California at Berkeley, Berkeley, CA, USA. [2]Department of Materials Science and Engineering, University of California at Berkeley, Berkeley, CA, USA. [3]Materials Sciences Division, Lawrence Berkeley National Laboratory, Berkeley, CA, USA. [4]Advanced Light Source, Lawrence Berkeley National Laboratory, Berkeley, CA, USA. [5]Department of Physics, University of Seoul, Seoul, South Korea. [6]Graduate Group in Applied Science and Technology, University of California at Berkeley, Berkeley, CA, USA. [7]National Institute for Materials Science, Tsukuba, Japan. [8]Molecular Foundry, Lawrence Berkeley National Laboratory, Berkeley, CA, USA. [9]Kavli Energy NanoSciences Institute, University of California at Berkeley and the Lawrence Berkeley National Laboratory, Berkeley, CA, USA. [10]These authors contributed equally: M. Iqbal Bakti Utama, Roland J. Koch and Kyunghoon Lee. ✉e-mail: jeiljung@uos.ac.kr; abostwick@lbl.gov; fengwang76@berkeley.edu

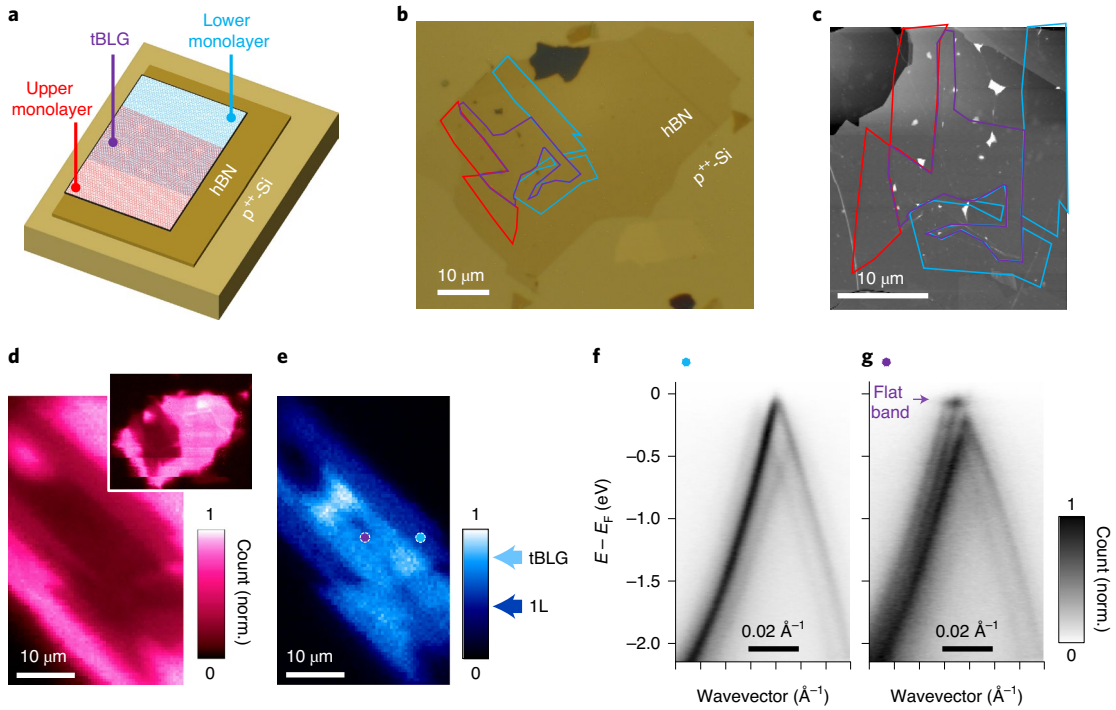

Fig. 1 | tBLG near magic angle twist on hBN substrate. a–c, Schematic illustration of the tBLG/hBN/doped Si sample (**a**), bright field optical micrograph (**b**) and AFM image of the sample (**c**). The boundary of each segment is indicated as follows: blue, lower graphene monolayer; red, upper graphene monolayer; purple: tBLG area. **d**,**e**, SPEM image generated from real space mapping of the valence band spectra and integrating the signal of hBN (**d**) and the signal of graphene (**e**). A larger area scan covering the entire hBN flake is given as the inset in **d**. The approximate intensity corresponding to monolayer and tBLG is marked in the colour scale of **e**. **f**,**g**, The energy-momentum band dispersion around the $\bar{K}$ point of lower graphene monolayer (**f**) and tBLG with local twist near magic angle (**g**). These spectra were measured at the locations marked with blue and purple circles in **e**. The flat band in **g** is indicated with a purple arrow.

Figure 1f,g shows the ARPES spectra collected from the lower graphene monolayer and the tBLG from locations as indicated in Fig. 1e. The monolayer spectrum shows the typical linear band dispersion characteristic for graphene and the sample is approximately charge neutral as the Dirac point is situated close to the Fermi level. Faint Dirac cone replicas are also seen surrounding the primary cone. The formation of these replicas is a result of the superlattice periodicity between hBN and graphene[25] (further details are discussed in Supplementary Fig. 4). On the other hand, the spectrum from the tBLG area shows a sharp feature near the Fermi level corresponding to the flat electronic band. Subsequent discussion will be focused on the tBLG data (microscopy in Fig. 2 and nanoARPES in Fig. 3) that are collected from this location.

It is important to fabricate the twist angle of the tBLG close to the first magic angle (~1°) as previous ARPES measurements on tBLG with other much smaller[20] or larger[19,26,27] twist angles did not observe any flat band signatures. Also, the twist angle in tBLG is sensitive to disorder, strain and temperature treatment that may alter the local twist angle from the intended design[6]. To confirm the local twist angle at tBLG sites where the flat band was observed in nanoARPES, we performed microwave impedance microscopy (MIM) imaging after completing the nanoARPES measurements (Fig. 2, also see Supplementary Fig. 3).

The MIM was measured exactly at the location where we observed the flat band from nanoARPES as shown in Figs. 1g and 3. This method, combined with the fact that MIM was done after nanoARPES, ensured that the twist angle that we determined represented the actual sample condition during the nanoARPES measurement. Inhomogeneity of the sample at other locations elsewhere is not an issue for our experiment. Likewise, the fabrication details and processing before the nanoARPES measurement (for example, the absence of top hBN and pre-nanoARPES annealing) are not relevant in the MIM imaging.

The imaginary part of the complex microwave response (MIM-Im) in general increases monotonically as a function of the local sample conductivity[28]. Therefore, MIM-Im serves as a viable means to probe the moiré superlattice as an alternative to topographic imaging (Supplementary Fig. 2) and to conductive AFM mode while not requiring grounding electrodes. Figure 2a shows the real space MIM-Im map of the tBLG location with the flat band feature. The MIM-Im signal presents a periodic modulation with sixfold rotational symmetry from the moiré pattern, a result of the misalignment of the constituent graphene monolayers. From the fast Fourier transform of the image (Fig. 2b), we can deduce an averaged real-space periodicity of 14.7 ± 0.4 nm, corresponding to a graphene/graphene twist angle of $\theta = (0.96 \pm 0.03)°$. Such periodicity can also be well-resolved directly in the line profile of the signal (Fig. 2c,d).

Figure 3 shows the photoemission spectra of the tBLG around the $\bar{K}$ points of the original Brillouin zone (BZ) from the constituent monolayers. The flat electronic bands are present near E_F, as also visualized experimentally along the various momentum cuts of the spectra in Fig. 3c–f. Here, the cutting geometries are shown as the inset in each panel following the schematic in Fig. 3a, where we also show the construction of the mini Brillouin zone (mBZ, in purple) of the tBLG from the original monolayer graphene BZs (red and blue). At the Fermi surface, the signal from the flat band is distributed around two intensity centres (Fig. 3b, top left). These distributions may originate from the states near the $\bar{K}$ point of the constituent upper and lower monolayer graphene, where the

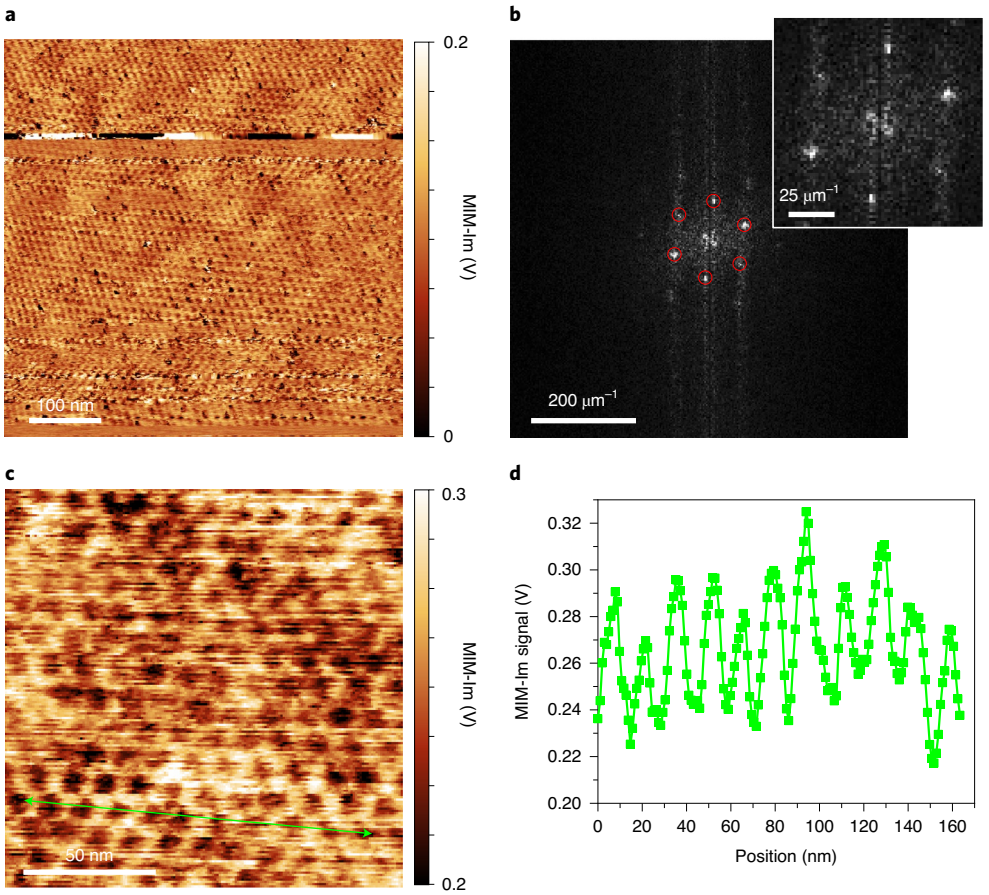

Fig. 2 | Moiré pattern visualized with MIM from tBLG in the location with flat electronic band feature. a,**b**, Wide area map of MIM-Im signal where the periodic moiré pattern is clearly visible (**a**). The fast Fourier transform of the image in **a** after excluding the horizontal scan artefact is shown in **b**. The red circles mark the position of first-order spots from the moiré period due to the graphene/graphene twist. Inset: zoom-in of the area around the first-order spots. **c**, A magnified view of the moiré pattern. **d**, MIM-Im signal profile taken along the green arrow in **c**.

features from the lower monolayer appear to be dimmer due to photoelectron attenuation[19].

Previous calculation of the band structure in magic angle tBLG predicted that the flat band feature should exist across the whole of the mBZ of the tBLG (ref. [3]). In agreement with the calculations, our nanoARPES measurement shows that the flat band subtends the entire area of the mBZ. This can be seen in Fig. 3b (top row), where the flat band feature at the Fermi surface covers the entire area of the mBZ (the mBZ size is shown as the purple hexagon in the insets of Fig. 3b for comparison). The flat band subtends a width of ~0.1 Å^{-1} along k_x, which is around twice as large as the $\bar{\kappa} - \bar{\gamma} - \bar{\kappa}'$ width of the mBZ of ~0.06 Å^{-1}. The wide momentum extent of the flat band is consistent with the strong real space localization of carriers occupying these states. Such extendedness of the flat band states, along with the small outgoing branches away from the $\bar{K}$ points, can also be reproduced in the ab initio-informed tight-binding simulation of the spectral function (Fig. 3b, top right). We have also eliminated the possibilities that the flat band in our tBLG originates from surface roughness (Supplementary Fig. 3), van Hove singularity around the hybridization gap (Supplementary Fig. 5), the bottom of the dispersing band (Supplementary Fig. 6), detector response issue and states from the graphene/hBN interface (Supplementary Fig. 7).

At higher binding energies, the equal energy cuts and the band dispersions also show the emergence of multiple Dirac cones. This observation indicates the hybridization of the Dirac cones of the two monolayers due to a strong interlayer coupling of the constituent monolayers, as is expected for small twist angles and the periodic repetition of the moiré mBZ. This is different from 'decoupled' bilayer graphene at large twist angles, where the band dispersion can be approximated by the two non-perturbed bands of the individual monolayers. Moreover, the periodic potential from the tBLG moiré superlattice is responsible for the avoided gaps that further split the bands[19]. Such emergence of extra bands away from the Fermi level has also been observed in other tBLG on non-hBN substrates[19,27], although in our sample the hybridized bands formed at lower binding energies due to the smaller twist angle.

Using the same choice of axes as for Fig. 3c,e, we performed a simulation of the spectral function and the results are shown in Fig. 3g,h (see Methods and the Supplementary Information for details). The simulated spectrum can reproduce qualitatively the salient features of the ARPES band dispersion, including the flat band at E_F and the emergence of multiple Dirac cones.

We compare the uniqueness of our flat band observation in tBLG relative to that in other graphitic systems in the following. Some of the previously observed flat state near the top of the valence band is based on multilayered rhombohedral stacking[12,15,17], in which the massive character of the state is explained by a model where the band edge dispersion decreases with increasing layer number. Several other studies[11,13,16] are based on epitaxial graphene on SiC(0001), where the degree of the band flatness is derived not from symmetry considerations but from the special environment of the substrate or doping coverage, thus creating a particular

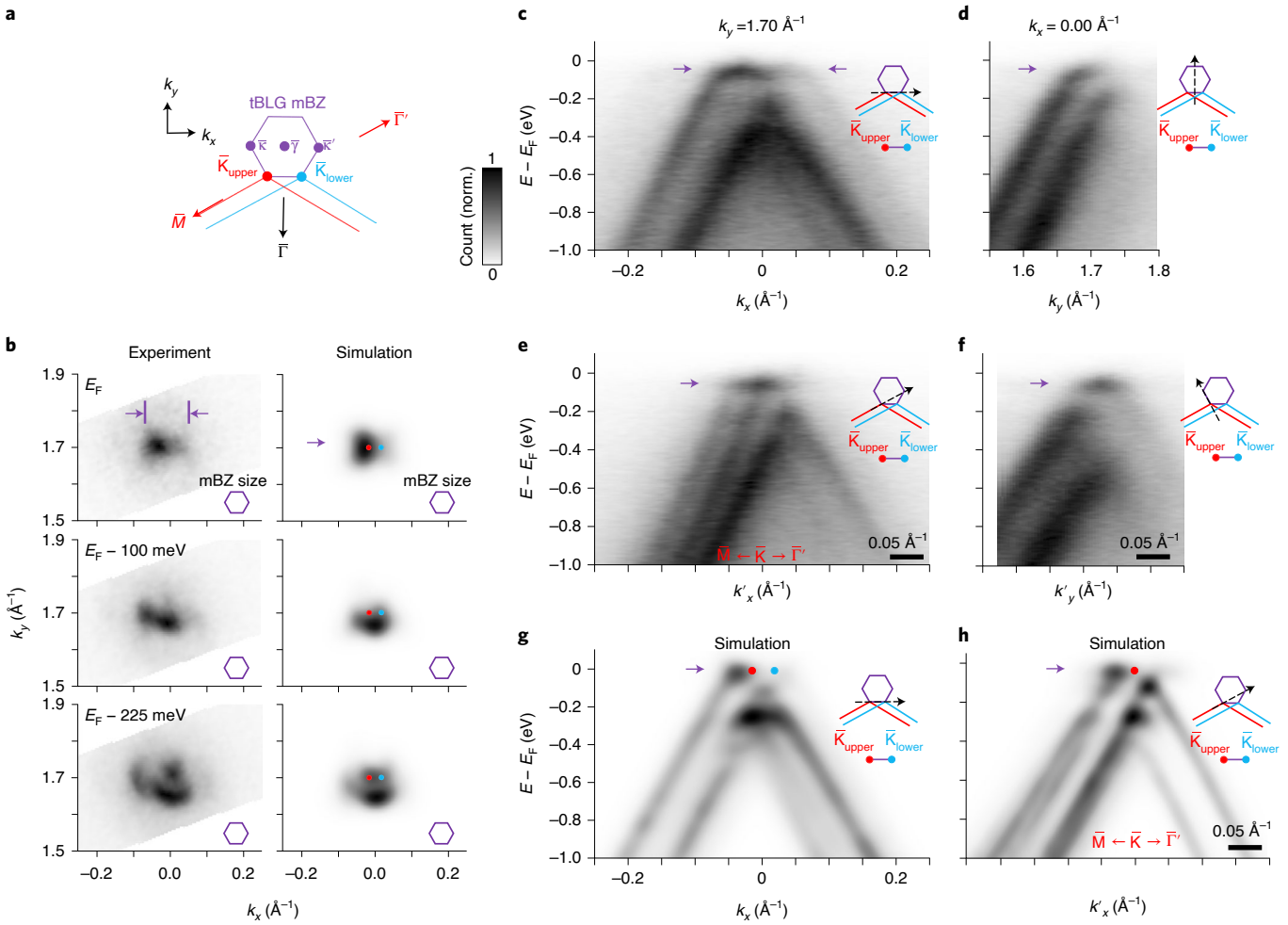

Fig. 3 | Electronic structure of tBLG and the visualization of the flat band dispersion. a, The geometry of the tBLG mBZ (purple hexagon) relative to the BZ of the original monolayers around the $\bar{K}$ point. The red and blue dots, as also superimposed in the simulation results in panels **b**, **g** and **h**, mark the locations of the original $\bar{K}$ points from the upper and lower monolayers, respectively. The origin of axis k_y is chosen to be along the $\bar{\Gamma} - \bar{\gamma}$ line. **b**, Equal energy cut for several binding energies. Images shown in the left and the right columns are the experimental and the simulation results, respectively. The to-scale size of the mBZ is represented by the purple hexagon at the lower right insets. **c**, The dispersion of the tBLG band along k_x at k_y=1.70 Å^{-1}. **d**, The dispersion of the tBLG band along k_y at k_x=0.00 Å^{-1}. **e**, An alternative view of the tBLG band along an axis k'_x that coincides with the path $\bar{M} - \bar{K} - \bar{\Gamma}'$ from the BZ of the upper monolayer. Here, $\bar{\Gamma}'$ is the centre of the nearest-neighbouring BZ. **f**, Band dispersion along an axis that is orthogonal to that in **e**. **g**,**h**, Simulated spectral functions of tBLG near the $\bar{K}$ point after accounting for lattice reconstruction. Panels **g** and **h** are visualizations along the momentum cut of k_x and k'_x, respectively, similar to the experimental spectra in panels **c** and **e**. In **c**–**h**, the direction of the momentum cut is illustrated in the inset of each panel. Additionally, the mBZ size (represented as the width along the $\bar{K}_{upper} - \bar{K}_{lower}$ direction) is also shown as the inset. The experiment and simulated images follow the colour scale shown near **c**. The flat electronic band is marked with purple arrows.

combination of hopping parameters and field gradient strength of the interface. Meanwhile, the flat band in tBLG arises from symmetry considerations due to the moiré potential from the twisting. The flat band in tBLG occurs only when the bilayer is twisted to magic angle (compare with Supplementary Fig. 5 for θ=3.5°). No uniform stacking order in bilayer graphene (for example AB or AA stacking) will give rise to a flat band. Such moiré physics is absent in the flat band of graphitic systems in previous studies. In particular, the moiré physics in magic angle tBLG has enabled the striking observations of novel correlated insulator states and superconductivity that are attributed to the emerging flat band and it has been the most active research topic in current condensed matter physics

Although detailed scanning tunnelling microscopy measurements have been performed on magic angle tBLG (refs. [6–9]), quasiparticle interference is only available for large angle tBLG (ref. [29]). A direct visualization of the flat band dispersion in a moiré superlattice using nanoARPES, such as that presented in our work, would therefore be beneficial for a more quantitative understanding of the moiré physics in magic angle tBLG. It is thus also of interest to perform detailed nanoARPES studies on other moiré superlattice-induced flat bands in related van der Waals heterostructure systems, including their behaviour at different filling factors with in situ electrostatic gating[30,31].

Online content

Any methods, additional references, Nature Research reporting summaries, source data, extended data, supplementary information, acknowledgements, peer review information; details of author contributions and competing interests; and statements of data and code availability are available at https://doi.org/10.1038/s41567-020-0974-x.

Received: 28 October 2019; Accepted: 19 June 2020;
Published online: 27 July 2020

References

1. Bistritzer, R. & MacDonald, A. H. Moiré bands in twisted double-layer graphene. *Proc. Natl Acad. Sci. USA* **108**, 12233–12237 (2011).
2. Suárez Morell, E., Correa, J. D., Vargas, P., Pacheco, M. & Barticevic, Z. Flat bands in slightly twisted bilayer graphene: tight-binding calculations. *Phys. Rev. B* **82**, 121407 (2010).
3. Cao, Y. et al. Correlated insulator behaviour at half-filling in magic-angle graphene superlattices. *Nature* **556**, 80–84 (2018).
4. Cao, Y. et al. Unconventional superconductivity in magic-angle graphene superlattices. *Nature* **556**, 43–50 (2018).
5. Li, G. et al. Observation of van hove singularities in twisted graphene layers. *Nat. Phys.* **6**, 109–113 (2010).
6. Kerelsky, A. et al. Maximized electron interactions at the magic angle in twisted bilayer graphene. *Nature* **572**, 95–100 (2019).
7. Xie, Y. et al. Spectroscopic signatures of many-body correlations in magic-angle twisted bilayer graphene. *Nature* **572**, 101–105 (2019).
8. Jiang, Y. et al. Charge-order and broken rotational symmetry in magic angle twisted bilayer graphene. *Nature* **573**, 91–95 (2019).
9. Choi, Y. et al. Electronic correlations in twisted bilayer graphene near the magic angle. *Nat. Phys.* **15**, 1174–1180 (2019).
10. Tomarken, S. L. et al. Electronic compressibility of magic angle graphene superlattices. *Phys. Rev. Lett.* **123**, 046601 (2019).
11. McChesney, J. L. et al. Extended van hove singularity and superconducting instability in doped graphene. *Phys. Rev. Lett.* **104**, 136803 (2010).
12. Pierucci, D. et al. Evidence for flat bands near the fermi level in epitaxial rhombohedral multilayer graphene. *ACS Nano* **9**, 5432–5439 (2015).
13. Marchenko, D. et al. Extremely flat band in bilayer graphene. *Sci. Adv.* **4**, eaau0059 (2018).
14. Senkovskiy, B. V. et al. Boron-doped graphene nanoribbons: electronic structure and raman fingerprint. *ACS Nano* **12**, 7571–7582 (2018).
15. Henck, H. et al. Flat electronic bands in long sequences of rhombohedral-stacked graphene. *Phys. Rev. B* **97**, 245421 (2018).
16. Ehlen, N. et al. Origin of the flat in heavily Cs-doped graphene. *ACS Nano* **14**, 1055–1059 (2019).
17. Bao, C. et al. Stacking-dependent electronic structure of trilayer graphene resolved by nanospot angle-resolved photoemission spectroscopy. *Nano Lett.* **17**, 1564–1568 (2017).
18. Lopes dos Santos, J. M. B., Peres, N. M. R. & Castro Neto, A. H. Graphene bilayer with a twist: electronic structure. *Phys. Rev. Lett.* **99**, 256802 (2007).
19. Ohta, T. et al. Evidence for interlayer coupling and moiré periodic potentials in twisted bilayer graphene. *Phys. Rev. Lett.* **109**, 186807 (2012).
20. Kim, K. S. et al. Coexisting massive and massless dirac fermions in symmetry-broken bilayer graphene. *Nat. Mater.* **12**, 887–892 (2013).
21. Yankowitz, M. et al. Tuning superconductivity in twisted bilayer graphene. *Science* **363**, 1059–1064 (2019).
22. Lu, X. et al. Superconductors, orbital magnets, and correlated states in magic-angle bilayer graphene. *Nature* **574**, 653–657 (2019).
23. Bultinck, N., Chatterjee, S. & Zaletel, M. P. Mechanism for anomalous hall ferromagnetism in twisted bilayer graphene. *Phys. Rev. Lett.* **124**, 166601 (2020).
24. Sharpe, A. L. et al. Emergent ferromagnetism near three-quarters filling in twisted bilayer graphene. *Science* **365**, 605–608 (2019).
25. Wang, E. et al. Gaps induced by inversion symmetry breaking and second-generation dirac cones in graphene/hexagonal boron nitride. *Nat. Phys.* **12**, 1111–1115 (2016).
26. Razado-Colambo, I. et al. Nanoarpes of twisted bilayer graphene on sic: Absence of velocity renormalization for small angles. *Sci. Rep.* **6**, 27261 (2016).
27. Peng, H. et al. Substrate doping effect and unusually large angle van hove singularity evolution in twisted bi- and multilayer graphene. *Adv. Mater.* **29**, 1606741 (2017).
28. Lai, K. et al. Nanoscale electronic inhomogeneity in In_2Se_3 nanoribbons revealed by microwave impedance microscopy. *Nano Lett.* **9**, 1265–1269 (2009).
29. Mallet, P., Brihuega, I., Cherkez, V., Gómez-Rodríguez, J. M. & Veuillen, J.-Y. Friedel oscillations in graphene-based systems probed by scanning tunneling microscopy. *C. R. Phys.* **17**, 294–301 (2016).
30. Joucken, F. et al. Visualizing the effect of an electrostatic gate with angle-resolved photoemission spectroscopy. *Nano Lett.* **19**, 2682–2687 (2019).
31. Nguyen, P. V. et al. Visualizing electrostatic gating effects in two-dimensional heterostructures. *Nature* **572**, 220–223 (2019).

Methods

Fabrication and structural characterization. We followed the tear-and-stack fabrication method to control the twist angle[32,33]. The step-by-step process is illustrated in Supplementary Fig. 1. We exfoliated a monolayer graphene and a 20 nm thick hBN flake on a Si substrate with 285 nm thick SiO_2 film. We then used a stamp with polypropylene carbonate (PPC) coating. All pick-up processes were performed at 45 °C. We first picked up the hBN with the stamp and used the flake to pick part of the monolayer graphene. The substrate, mounted on a rotation stage, was then rotated by an angle of ~1.1°. The remaining monolayer segment was then picked up to overlap with the monolayer already on the hBN, producing a tBLG. The PPC film was peeled from the stamp and transferred onto a clean highly doped Si substrate. Finally, the sample was annealed in vacuum at 250 °C for 3 h to remove the PPC film.

NanoARPES measurement. The sample was transported to the Microscopic and Electronic Structure Observatory (MAESTRO) at the Advanced Light Source where it was inserted in the nanoARPES UHV endstation with a base pressure lower than 5×10^{-11} mbar. The sample was annealed at 150 °C for 24 h prior to the measurement in order to desorb adsorbates. The nanoARPES measurement was performed with capillary focusing using a photon energy of 95 eV (except for Supplementary Fig. 4a–d which was measured at 147 eV) and a beam spot size of approximately 1 μm. The data were collected using a hemispherical Scienta R4000 electron analyser. The net energy resolution of the nanoARPES data was around 34 meV. All measurements were carried out at room temperature.

Scanning probe microscopy. After completing the nanoARPES measurement, the sample was collected and MIM measurement was performed at ambient conditions without re-annealing to preserve the twist angle and the sample condition. The MIM characterization was carried out with a modified Asylum MFP-3D AFM with commercial ScanWave electronics and coaxially shielded probes (PrimeNano Inc)[34]. A microwave frequency of 2.9 GHz was sent to the tip followed by the collection of the reflected signals. The MIM signal was measured concurrently with the topographic imaging. The MIM measurement was conducted in contact mode with sub-10 nm lateral resolution. Additional AFM imaging to measure the topography was also performed with Asylum Cypher VRS and Park NX-10 instruments.

Spectral function simulation. The unfolded band structure of tBLG was calculated using a tight-binding model informed from ab initio density functional theory calculations for the atomic and electronic structures. A twist angle of 0.97° containing a total of 14,288 atoms in the supercell was used in the simulation. The atomic structure calculation included the relaxation effects through LAMMPS molecular dynamic simulations[35] using force fields tailored to reproduce ab initio total energies for different local stacking configurations[36–38]. For the electronic structure we used an effective nearest neighbour hopping energy of $|t_0| \sim 3.1$ eV corresponding to a Fermi velocity of $\sim 1.05 \times 10^6$ m s^{-1} within the F2G2 model[39] for the intralayer hopping terms in graphene. Our model for the interlayer coupling for the atomic relaxation and tight-binding electronic structures was designed to give the bandwidth minimum near ~1.05° (evidence for lattice relaxation in minimally twisted tBLG from a similar sample fabrication method is available in Supplementary Fig. 8 and see Supplementary Fig. 9 for the band structure in the folded-zone scheme). The spectral function calculation followed the theory and band-unfolding scheme described previously[40], with the spectrum projected onto the BZ of the lower graphene monolayer. To reproduce the asymmetry in the spectral function intensity owing to the upper and lower monolayer graphene, we assigned an intensity weight ratio of 2:1 in the calculation. The spectral function also accounted for the Fermi–Dirac distribution to reproduce the broadening near E_F. The equal energy cut was displayed by incorporating post-processing Gaussian broadening of the momentum space and a cutoff energy of ±20 meV around the Fermi level in energy space.

Data availability

The data that support the plots within this paper and other finding of this study are available from the corresponding author upon reasonable request. Simulation parameters are provided in the Supplementary Information and can be used as in LAMMPS or with the KIM MD potential database.

References

32. Kim, K. et al. van der Waals heterostructures with high accuracy rotational alignment. *Nano Lett.* **16**, 1989–1995 (2016).
33. Cao, Y. et al. Superlattice-induced insulating states and valley-protected orbits in twisted bilayer graphene. *Phys. Rev. Lett.* **117**, 116804 (2016).
34. Lai, K., Kundhikanjana, W., Kelly, M. A. & Shen, Z.-X. Nanoscale microwave microscopy using shielded cantilever probes. *Appl. Nanosci.* **1**, 13–18 (2011).
35. Plimpton, S. Fast parallel algorithms for short-range molecular dynamics. *J. Comp. Phys.* **117**, 1–19 (1995).
36. Leconte, N., An, J. J., Javvaji, J. & Jung, J. Relaxation effects in twisted bilayer graphene: a multiscale approach. Preprint at https://arxiv.org/abs/1910.12805 (2019).
37. Wen, M., Carr, S., Fang, S., Kaxiras, E. & Tadmor, E. B. Dihedral-angle-corrected registry-dependent interlayer potential for multilayer graphene structures. *Phys. Rev. B* **98**, 235404 (2018).
38. Leconte, N., Jung, J., Lebègue, S. & Gould, T. Moire-pattern interlayer potentials in van der waals materials in the random-phase approximation. *Phys. Rev. B* **96**, 195431 (2017).
39. Jung, J. & MacDonald, A. H. Accurate tight-binding models for the π bands of bilayer graphene. *Phys. Rev. B* **89**, 035405 (2014).
40. Ku, W., Berlijn, T. & Lee, C.-C. Unfolding first-principles band structures. *Phys. Rev. Lett.* **104**, 216401 (2010).

Acknowledgements

We thank S. Kahn for technical assistance in the sample fabrication setup. This work was supported as part of the Center for Novel Pathways to Quantum Coherence in Materials, an Energy Frontier Research Center funded by the US Department of Energy, Office of Science, Basic Energy Sciences. The Advanced Light Source is supported by the Director, Office of Science, Office of Basic Energy Sciences, of the US Department of Energy under contract no. DE-AC02-05CH11231. The MIM measurements were supported by the Materials Sciences and Engineering Division of the US Department of Energy under contract no. DE-AC02-05-CH11231 (sp2-Bonded Materials Program KC2207). The MIM instrument at the Molecular Foundry was supported by the Office of Science, Office of Basic Energy Sciences, of the US Department of Energy under contract no. DE-AC02-05CH11231. Support for K.W. and T.T. from the Elemental Strategy Initiative, conducted by the MEXT, Japan and CREST (JPMJCR15F3) is acknowledged. J.S.T. and N.L. acknowledge the Korean National Research Foundation grant no. NRF-2018R1C1B6004437 and the Korea Research Fellowship Program funded by the Ministry of Science and ICT (KRF-2016H1D3A1023826), as well as the computational resources by KISTI through grant no. KSC-2018-CHA-0077. J.J. was supported by the Samsung Science and Technology Foundation under project SSTF-BAA1802-06.

Author contributions

F.W., E.R. and M.I.B.U. conceived the project. M.I.B.U. developed the sample preparation method and carried out sample fabrication with the assistance of J.Z. The nanoARPES experiments were performed by R.J.K., A.B. and E.R. The nanoARPES setup was developed and maintained by R.J.K., C.J., A.B. and E.R. The nanoARPES experimental data were analysed by M.I.B.U. and F.W. with A.B. and E.R. providing guidance. K.L. contributed to the MIM instrumentation setup. K.L. and M.I.B.U. performed AFM and MIM and analysed the data with P.D.A., A.W.B. and A.Z. providing guidance. J.J. and N.L. calculated the spectral functions. H.L. and S.Z. contributed to the surface cleaning process. L.J. performed scanning near field optical microscopy. K.W. and T.T. grew the hBN single crystal. F.W. and E.R. supervised the project. M.I.B.U. and F.W. wrote the manuscript with input from all authors.

Competing interests

The authors declare no competing interests.

Additional information

Supplementary information is available for this paper at https://doi.org/10.1038/s41567-020-0974-x.

Correspondence and requests for materials should be addressed to J.J., A.B. or F.W.

Reprints and permissions information is available at www.nature.com/reprints.